



## Full length article

## Bidirectional payload enhancement of soft actuator via nested dual-chamber origami structure

Xiaohuang Liu<sup>a</sup>, Zhonggui Fang<sup>a</sup>, Shaowu Tang<sup>a</sup>, Fang Chen<sup>a</sup>, Dihan Liu<sup>a</sup>, Sicong Liu<sup>b,c</sup>,\*, Juan Yi<sup>d</sup>, Hongqiang Wang<sup>a</sup>, Zheng Wang<sup>a</sup>, Jian S. Dai<sup>a</sup>\*\*

<sup>a</sup> Department of Mechanical and Energy Engineering, Southern University of Science and Technology, Shenzhen, Guangdong, 518000, China

<sup>b</sup> Sino-German College of Intelligent Manufacturing, Shenzhen Technology University, Shenzhen, Guangdong, 518055, China

<sup>c</sup> Guangdong Provincial Key Laboratory of Intelligent Morphing Mechanisms and Adaptive Robotics, Harbin Institute of Technology (Shenzhen), Shenzhen, Guangdong, 518055, China

<sup>d</sup> School of Advanced Engineering, Great Bay University, Dongguan, Guangdong, 523000, China

## ARTICLE INFO

## Keywords:

Soft actuator  
Origami structure  
Theoretical analysis  
Dual-chamber  
Bidirectional payload  
Curved crease

## ABSTRACT

Pneumatic soft robots offer promising solutions for safe human–robot interaction and exploration tasks in unstructured environments. However, compared with the positive pressure ( $\gg 1$  atm) input, the limited driving capacity of the negative pressure ( $< 1$  atm) input restricts the bidirectional payload output performance of the soft pneumatic actuators (SPAs). In this paper, we propose the nested dual-chamber origami (NDO) structure which enables the bidirectional compounding actuation, i.e. applying positive and negative pressure input simultaneously to generate linear motions in opposite axial directions, to enhance the SPA's bidirectional payload performance. Based on the analysis on the correlation of the symmetries and the motion modes of the soft origami chambers, a linear NDO actuator is constructed by coaxially nesting the external Yoshimura origami (EYO) chamber and the internal Pleated origami (IPO) chamber. The quasi-static models of the chambers are derived to present the NDO deformations. The resisting force of curved convergent creases is derived by defining the proportional relation between the length of the folding region and width of the origami facet based on the small-strain folding (SSF) principle. The theoretical models are validated by the mechanical behaviors of the 3D-printed NDO actuator in experiments and the payload enhancement is verified. The average enhancement of the contraction force (and elongation force) of the NDO actuator reaches 101.7% (and 70.5%) over the single-chamber EYO actuator and 21.2% (and 19.7%) over the sum of independent single-chamber EYO actuator and IPO actuator. The practicality of the NDO actuator is verified by driving a compact gripper with high payload performance in both gripping and stretching motions. The bidirectional enhancement with compact design will promote the development and application of soft pneumatic actuators.

## 1. Introduction

Soft pneumatic robots, due to the advantages of compliance, adaptability and simple actuation [1], attract broad interest fields including medical rehabilitation [2,3], human enhancement [4], exploration of unstructured environments [5–7], universal grippers [8,9] and bionic robots [10–12]. Soft pneumatic actuators (SPAs) working as the core component of such robots, predominantly determine the robotic system's performance, therefore have received extensive explorations on diverse aspects, such as the motion modes [13–17], perception [18–20], variable stiffness [21,22], embedded fluidic control circuits [23,24] and sustainable fabrication [25,26]. These extensive and detailed researches have led to a significant improvement in the performance of such

actuators, and thereby broadening the application boundaries of soft pneumatic robots.

The payload capability, as one of the most important properties of SPAs, is considered as a pivotal requirement in constituting soft robotic arms [27] and grippers [28,29], and in applications such as the rescue operation [30]. However, due to the inherent softness of materials and structures, a substantial portion of the input energy is consumed by the in-plane stretching of the materials and the output force in undesirable directions, which limits the output performance in the desired direction [31]. Many researches proposed methods to enhance the payload performance of SPAs, including the following three main aspects: (1) Increase the scale of the actuator by leveraging the advantage of easy

\* Corresponding author at: Sino-German College of Intelligent Manufacturing, Shenzhen Technology University, Shenzhen, Guangdong, 518055, China.

\*\* Corresponding author.

E-mail addresses: [liusicong@sztu.edu.cn](mailto:liusicong@sztu.edu.cn) (S. Liu), [daijs@sustech.edu.cn](mailto:daijs@sustech.edu.cn) (J.S. Dai).

fabrication [32,33]. (2) Employ the soft-rigid coupled structural design to guide the output force in desired direction [34–36]. (3) Increase the stiffness of the material to restrict excessive inflation and to bear high pressure, thereby more energy can be concentrated in the desired deformations [37,38]. For example, Li et al. [33] presented a fluid-driven origami-inspired artificial muscle which can be easily fabricated in multiscale. Dong et al. [36] proposed a soft-rigid coupled linear actuator that prevent the soft skin from buckling to achieve increased axial output force. Long et al. [38] proposed an elastic-soft hybrid pneumatic actuator that composed of PLA-CF sheets and TPU-coated fabric to reduce the energy loss caused by the hyperelastic materials.

Among the available methods, the origami-inspired SPA (OSPA), which obtains output by the design of folding creases [39–41], is considered as a promising method to enhance the payload capacity utilizing the reinforcement of the origami structure. The OSPA exhibits a remarkable ability to guide the output force through the strategic layout of the creases [42,43]. It generates large displacements mainly via folding deformations rather than the material's in-plane stretching, which allows for the utilization of soft materials with higher stiffness [44] to significantly restrict the undesired deformations and mitigate energy loss. Furthermore, the thin-walled structures of OSPAs can be straight-forwardly fabricated with scalability, which enables them to maintain high specific power at large scales [32,45].

Although the state-of-the-art methods effectively improved the payload capacity of the single-chamber SPAs, challenge still remains in achieving bidirectional high payload performance. As shown in Fig. 1a, due to the disparity between the negative and positive pressures, the pneumatic actuation imposes limitations to generate high payloads simultaneously in opposite directions. The maximum relative negative pressure is around 1 atm, while the positive theoretically has almost no limit, such disparity greatly limits the performance in direction driven by the negative pressure. In order to reduce energy loss, the airtight chambers are usually designed to be thin-walled structures, causing the buckling failure under large negative pressure input which leads to reduced lifespan and undesired motions. To avoid this, the negative pressure value is limited in the soft robotic actuation, which further constrains the payload performance.

To enhance the SPA's bidirectional payload performance by utilizing compounding pressure actuation, i.e. applying positive and negative pressure simultaneously to drive the SPA in the opposite directions, feasible approaches have been put forward : (1) Connecting two actuators in series to enable bidirectional rotations through compounding pressure actuation [46,47]. (2) Placing multiple chambers in parallel externally to facilitate bidirectional bending motions [48–50]. For example, Yi et al. [47] proposed an origami soft robotic joint that antagonistically actuates two rotary origami chambers using compressed air for joint rotation, which obtained a much higher torque-to-weight ratio compared with commercial servo motors. Lee et al. [50] presented a soft pneumatic bending actuator which consisted of three chambers and was able to perform omnidirectional bending deformation with high output force. Although these approaches have successfully enhanced the bidirectional payload capability of SPAs for rotational and bending motions, respectively, they encounter limitations when utilized for typical linear SPAs. The method of connecting actuators in series inevitably introduces extra matching components, which limits the potential to achieve a compact design. The method following the external parallel design is difficult to realize linear bidirectional payload enhancement.

Researches on the modeling of the SPAs promote soft robotic applications by predicting and hence controlling the output of the robots [51–54]. Existing researches on OSPA have provided numerous kinematic and mechanical models for describing the origami units' behavior [55]. Kinematics-based analysis represents the origami structures using creases folding angles as variables. It is first to determine the constraint conditions, such as the developable, flat-foldable, and loop closure constraint [56,57]. Then, Kinematic models that reveal the trajectories of the panels based on the constraints are developed

by different mathematic methods like the spherical trigonometry [58], Denavit–Hartenberg transformation matrix [59] or quaternions [60]. Mechanics-based analysis is used to simulate the physical behaviors of the origami structures due to applied loading, self-folding, or other external effects. Generic mechanical models include Finite Element (FE) Models [61,62], and reduced-order models like bar and hinge models [63,64] and plate theory based models [65,66]. The FE models can analyze the specific mechanical behavior of structures with extremely high precision, even in the buckling state of the origami structures, but are also a time-consuming “black box”, making it difficult to reveal the theoretical behaviors of the origami structures. The bar and hinge method represents an origami pattern using bar and rotational spring elements, without considering the local effect around the boundary edges. The plate theory based method introduces additional rotational springs to the connection between the origami panels and the compliant creases for detailed deformation representation. Existing studies have primarily focused on the behaviors of origami structures with straight creases, or the developable curved creases [67–69], while the origami structure with curved convergent creases has yet to be systematically investigated.

In this paper, we proposed the nested dual-chamber origami-inspired (NDO) structure, which enables bidirectional compounding pressure actuation, to enhance the bidirectional payload performance of SPA. By combining the small-strain folding (SSF) principle [70] for foldable structures and the kinematic assumptions, a theoretical analysis on the origami structure with curved convergent creases was conducted. The main contributions of this paper are summarized as follows:

- (1) According to the analysis between the structural symmetries and motion modes, the NDO structure was proposed by coaxially nesting the external Yoshimura origami (EYO) chamber and the internal Pleated origami (IPO) chamber, to enhance the linear bidirectional payload performance of SPAs by compounding pressure actuation. Both chambers meet the point, axial and plane symmetry, and generate opposite axial translations under same input pressure state.
- (2) The quasi-static model was derived and validated to present the NDO structure's mechanical behaviors and to estimate the payload enhancement capability. The resisting force of the curved convergent creases of the IPO chamber are derived based on the SSF principle by redefining the proportional relationship between the length of the folding region and the width of the facet.
- (3) Prototype of the NDO actuator was designed and fabricated to verify the quasi-static models and the effectiveness of the NDO enhancement. Actuated by the opposite axial motions of single NDO actuator, a compact one degree-of-freedom (DOF) gripper with both high gripping and stretching forces was constructed to validate the practicality in soft robotic application.

## 2. Concept of the NDO structure

The origami structures of OSPAs offer insights into potential solutions for payload limitation in the direction actuated by negative pressure. The origami structures, which are capable of achieving various motion modes from programming the accumulation of crease folding, are able to construct origami chambers that generate linear motions in opposite directions under same pressure state. Chambers that generate elongation or contraction motion under positive pressure state achieve large payload in corresponding direction, achieve limited payload in the reverse direction under negative pressure (Fig. 1a). By coaxially nesting two types of chambers, the NDO structure that generates bidirectional motion with compounding pressure actuation can be created. As the bidirectional motion of the NDO actuator is generated by applying opposite relative pressure to the two chambers simultaneously, e.g., positive pressure in the external chamber and

negative pressure in the inner chamber when output elongation, and negative in the external and positive in the inner when output contraction, the payload limitations existing in the direction actuated solely by negative pressure can be avoided, thereby achieving bidirectional payload performance.

To construct the bidirectional payload enhanced airtight chamber with origami structure, it is necessary to clarify the relationship between the kinematic behaviors of the soft origami chambers and the corresponding structural characteristics. Unlike rigid structures, which achieve motion through kinematic pairs at the joints of moving components, soft origami structures generate motion by deforming the soft material, such as the bending around the creases. The motion depends not only on the specific configuration of the origami structure but also the properties of the soft material, which is a highly coupled process integrating kinematics and mechanics. This complexity makes it extremely challenging to represent the motions with explicit analysis. Conversely, if the origami chambers conform to certain structural symmetry, the analysis of their motion modes can be substantially simplified.

The geometric symmetries of OSPAs, including point, axial and plane symmetry, not only simplifies the mechanical analysis of the origami chambers by decomposing the chamber into identical segments, but also imposes constraints on their motion modes. The constraints during the deformation process can be described by the following principles: (1) For point symmetry, planes symmetric about a point remain parallel. (2) For axial symmetry, the line segments connecting points symmetric about an axis remain perpendicular and intersect with the symmetry axis. (3) For plane symmetry, the line segments connecting points symmetric about a plane remain perpendicular to the symmetry plane.

Depending on the constraints of symmetries, the active motion modes of OSPAs can be characterized by whether there is symmetric point, or whether there is symmetric plane or axis that is perpendicular to the relative planes. The correspondence is summarized in Fig. 1c. When the chamber conforms to single symmetry, its motion mode is determined by such symmetric constraint. Chambers with point symmetry generate purely spatial translations (vii). Chambers with axial symmetry perform twisting motion around the symmetric axis, e.g., (ix) the Kresling chamber. Chambers with plane symmetry generate bending or rotation around axes perpendicular to the symmetric plane, e.g., (i, ii) the variants of Yoshimura chamber. When the chamber conforms to multiple symmetries, its motion mode is determined by the combination of the symmetric constraints. As shown in Fig. 1c, chambers with point-plane symmetry can only undergo translation along the direction vectors that define the symmetric plane, e.g., (iii) combination of the variant of Yoshimura chambers. Chambers with point-axial symmetry (or plane-axial symmetry) execute linear motion along the symmetric axis, such as (viii) the combination of two mirrored Kresling chambers [40] (or (iv) the cropped Yoshimura variant). Chambers that conform to all three symmetric conditions realize linear motion along the symmetric axis, e.g., (v) the Pleated chamber [32,71] and (vi) the Yoshimura chamber [4,39]. These analyses of the motion modes in soft origami chambers benefit the design of OSPAs.

According to the demand of bidirectional performance enhancement, we designed the NDO actuator with the EYO chamber and the IPO chamber which meet all symmetric conditions (Fig. 1d). The EYO chamber generates linear elongation motion when inflated and contraction when deflated, which is developed by stacking and circularly patterning parallel straight creases. The IPO chamber generates linear contraction motion when inflated and elongation when deflated, which is developed by circularly patterning curved convergent creases. The linear motion of IPO chamber is generated by the pressure difference of the lateral folding pleats, while the linear motion of EYO chamber is mainly generated by the pressure difference of the end surfaces. Thus, constructing the NDO actuator by nesting IPO chamber within the EYO chamber is able to enhance the payload performance inherently.

**Table 1**  
Design parameters of the EYO chamber.

Geometry parameter	Value
Young's modulus $E$	30 MPa (TPU95A)
Thickness $t_Y$	0.75 mm
Height $H_{Y0}$	58 mm
Folding units in one layer	2
Folding layers $v$	3
Edges of trapezoid facet $a, b, c$	50, 72, 18.23 mm
Angle of trapezoid $\alpha$	52.88°
Width of trapezoid facets $L_{Y0}$	14.53 mm
Angle at horizontal crease $\theta_0$	81.63°
Angle at vertical crease $\varphi_0$	304.94°

As a result, the integrated NDO actuator generates elongation force by applying positive pressure to the EYO chamber and negative pressure to the IPO chamber, and generates contraction force by applying positive to IPO chamber and negative to EYO (Fig. 1e). This nested design effectively enables the utilization of compounding actuation, and levitates the payload limitations. In the following contents, we will undertake theoretical modeling and experimental verification to assess the payload enhancement capabilities of the NDO structure.

### 3. Modeling of the NDO actuator

The kinematic and mechanical models of SPAs serve as the foundation for predicting their behavior and provide design guidance for the geometric parameters, which are essential in the further design and application of soft robots. In this section, we derive the quasi-static model of the NDO actuator based on the geometric configuration and parameters of both chambers, revealing the relationships between air pressure, displacement, and output force.

The output force of the NDO actuator can be basically divided into two types of forces: the axial resisting force generated by the stiffness of the chambers and the axial active force generated by the pressure difference. Therefore, the output force of the NDO actuator can be derived as

$$F_{\text{NDO}} = F_Y + F_P = F_{YR} + F_{YA} + F_{PR} + F_{PA}, \quad (1)$$

where  $F_{PR}$  and  $F_{YR}$  are the resisting forces of the IPO chamber and the EYO chamber, respectively.  $F_{PA}$  and  $F_{YA}$  are the active forces of the IPO chamber and the EYO chamber, respectively.  $F_Y = F_{YR} + F_{YA}$  is the output force of the EYO chamber, and  $F_P = F_{PR} + F_{PA}$  is the output force of the IPO chamber.

According to the Eq. (1), the output force of the NDO actuator is directly related to four component forces. The remainder of this section addresses how to analyze each of these forces in two chambers separately.

#### 3.1. Modeling of the EYO chamber

The resisting force of the EYO chambers is related to the bending deformation around the creases and the tensile deformation of the facets, which has been verified in the previous work using the SSF principle [70]. Here, we consider a quadrilateral cross-section chamber design, as shown in Fig. 2a. According to the SSF principle, deformation of the origami structure can be analyzed as a cantilever beam being bent at the adjacent area of the creases and stretched along the facets. The bending region and the in-plane tension displacement of the actuator are expressed as  $nt$  and  $\frac{m\Delta h}{2}$  (Fig. 2b), where the coefficients  $n$  and  $m$  that indicate the bending region and stretching extent of EYO chamber can be calibrated experimentally. By incorporating the static analysis of combined bending and tension deformations, the relationship between resisting force  $F_{YR}$  and the height of EYO chamber  $H_Y$  can be derived as Eq. (2).

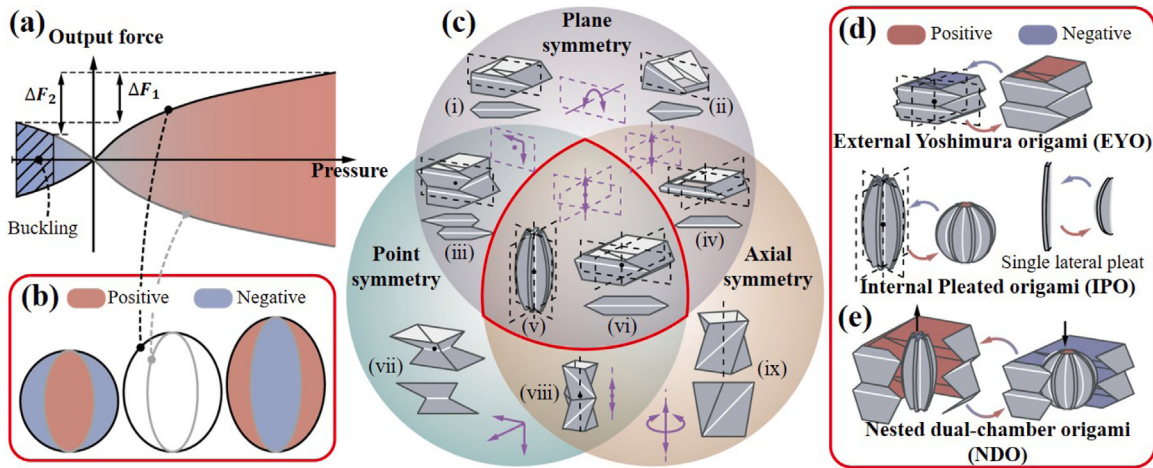


**Fig. 1.** The concept of the nest dual-chamber origami-inspired (NDO) structure. (a) Limitation in SPA to generate high payloads simultaneously in opposite directions, due to the disparity between the negative and positive pressures. (b) The NDO structure achieves bidirectional payload enhancement of linear SPAs by the compounding pressure actuation. (c) The symmetric configuration of the single-chamber origami structures simplify the theoretical analysis and simultaneously determines their active kinematic behaviors. ((i) and (ii) the variants of Yoshimura chamber; (iii) combination of the variant of Yoshimura chambers; (iv) the cropped Yoshimura variant; (v) the Pleated chamber; (vi) the Yoshimura chamber; (vii) Chamber with point symmetry; (viii) the combination of two mirrored Kresling chambers; (ix) the Kresling chamber.) (d) By coaxially nesting two kinds of origami-inspired chambers which satisfy all the symmetric conditions and perform opposite motions under same pressure states (e) the linear NDO actuator is constructed.

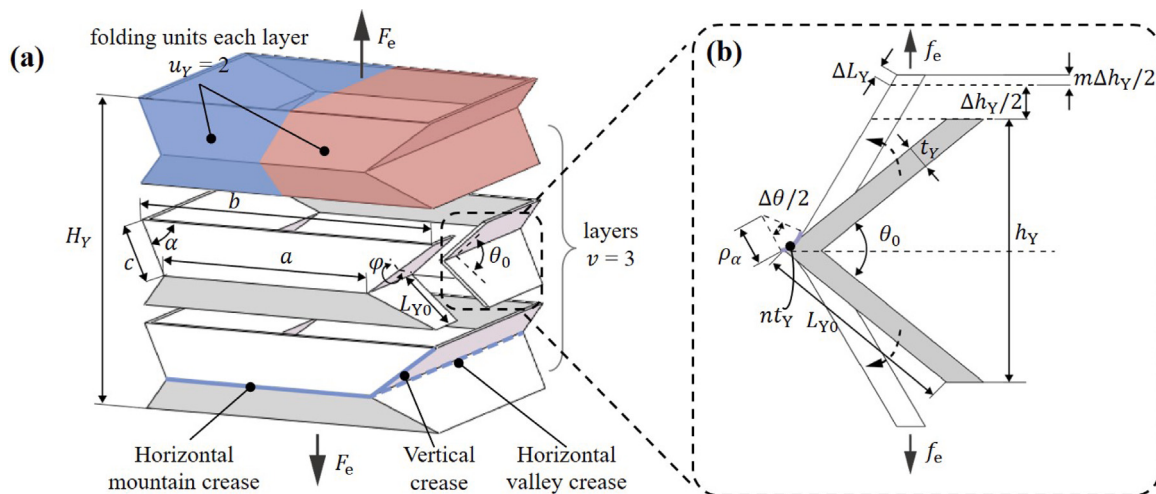


**Fig. 2.** The analysis of the resisting force of typical EYO chamber  $F_{YR}$  based on the small-strain folding (SSF) principle. (a) The EYO chamber with three layers with the cross-section in the shape of a rectangle,  $F_e$  is the input force acting in both sides of EYO chamber. (b) When subjected to external force  $f_e$ , the resisting force is generated by tensile stress due to the in-plane stretching of the facets, together with the bending moments generated by bending deformation at the folding region, i.e. the adjacent area of the facets along the creases.

$$F_{YR} = \frac{uv(a+b)Et_Y^2}{6n(H_Y - H_{Y0})} \left( \arcsin\left(\frac{H_Y}{2vL_{Y0}}\right) - \arcsin\left(\frac{H_{Y0}}{2vL_{Y0}}\right) \right)^2 + \frac{2uvEt_Y(a+b)L_{Y0}}{H_Y - H_{Y0}} \left( m - \frac{mH_{Y0}}{H_Y} - \ln\left(1 + m - \frac{mH_{Y0}}{H_Y}\right) \right) + \frac{uvct_Y^2}{3n(H_Y - H_{Y0})} \left( \arcsin\left(\frac{H_Y}{\tan\alpha\sqrt{4v^2c^2 - H_Y^2}}\right) - \arcsin\left(\frac{H_{Y0}}{\tan\alpha\sqrt{4v^2c^2 - H_{Y0}^2}}\right) \right)^2 \quad (2)$$

The specific meaning of the parameters  $H_{Y0}$ ,  $a$ ,  $b$ ,  $c$ ,  $u$ ,  $v$ ,  $t_Y$ ,  $\alpha$  and  $L_{Y0}$  are defined in Table 1. Parameters ending with a subscript '0' (e.g.,  $H_{Y0}$ ) correspond to the initial conditions. It can be observed

from the formula that once the design parameters of the EYO structure are established, the resisting force is solely dependent on the height of the structure during deformation.

The active force of airtight chamber can be derived from the equilibrium relationship between the work done by the active force and the energy generated by the pressure difference in the quasi-static state. It can be derived as

$$F_A = P \frac{dV}{dH} = PS, \quad (3)$$

where  $F_A$  and  $V$  represents the active force and volume of the chamber with inner pressure  $P$  at height  $H$ .  $S = \frac{dV}{dH}$  is considered as the equivalent area of the chamber.

According to [28], the volume of typical EYO chamber can be simplified to be a linear function of the length of the chamber. Therefore, the active force of the EYO chamber  $F_{YA}$  can be expressed as

$$F_{YA} = P_Y S_Y, \quad (4)$$

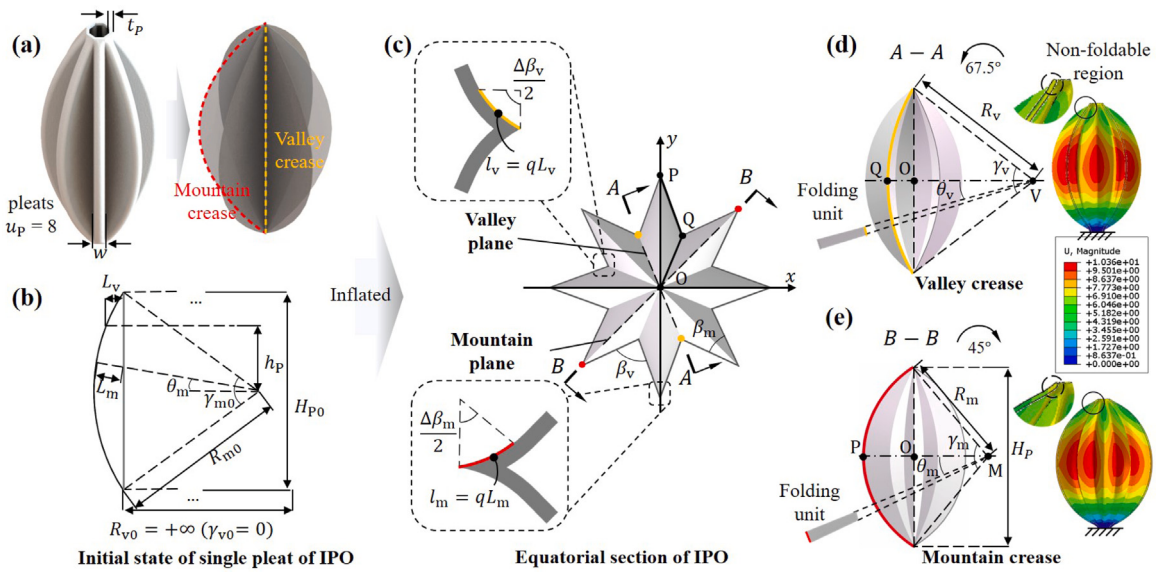


**Fig. 3.** The analysis of the resisting force of typical IPO chamber. (a) The IPO chamber is abstracted into a thin-walled structure with little impact of the membrane thickness during deformation. (b) Parameters of the outline of the pleat in the initial state, including definition of the width of the facets, initial radius of the creases and the corresponding central angle. (c) The equatorial section of the IPO chamber and bending deformation near the valley and mountain creases. (d) and (e) are the deformation state of the valley creases and mountain creases observed on the mountain plane and valley plane defined in the equatorial section of the IPO chamber.

where the equivalent area of the EYO chamber  $S_Y$  is a constant which can be calibrated experimentally.  $P_Y$  is the relative pressure in the EYO chamber.

So far, we have completed the analysis and modeling of the resisting force and active force of the EYO chamber. Next, we will proceed to analyze and model the IPO chamber.

### 3.2. Modeling of the IPO chamber

A typical IPO structure contains several identical arc-shaped pleats ( $u_p = 8$  in Fig. 3). During the pressurization process of actuation, the valley folds of the lateral folding pleats gradually bulges outward to occupy the space created by the expanding radial distance. To derive the reduced-order model of the IPO chamber that reveals the theoretical relation between the geometric parameters and the deformation of the folding pleats, the kinematic behavior of the IPO chamber is simplified as unfolding the lateral pleats with minimum thickness (Fig. 3a). Inspired by the SSF principle, which analyzes the deformation of the origami structure efficiently, the unfolding motion of the curved convergent creases is treated as a cantilever beam being bent at the adjacent region around the crease, while the length of the folding region  $l_v$  and  $l_m$  is treated to be proportional to the width of the facets (Fig. 3c), which avoids the situation that the theoretical length of the folding region is greater than the width of the facets. The mountain creases and valley creases are assumed to maintain in arc shape, without changing their length. The inner crease, which is initially straight, can be regarded as an arc with a central angle of  $0^\circ$  and infinite radius. The folding angle along the crease is assumed to be the same as the folding angle on the equatorial section. To unify the output force analysis of the NDO actuator in the axial direction, the resistance of the IPO chamber is transformed into the pseudo resisting force  $F_{PR}$  along the axial direction based on the principle of virtual work as

$$F_{PR} = \frac{\int M_m d\beta_m + \int M_v d\beta_v}{dH_p}, \quad (5)$$

where  $M_m$  and  $\beta_m$  are the out-of-plane bending moment and the folding angle of the mountain creases, respectively.  $M_v$  and  $d\beta_v$  are the out-of-plane bending moment and the folding angle of the valley creases, respectively.  $H_p$  is the height of the IPO chamber.

We first derived the folding angle of the creases,  $\beta_m$  and  $\beta_v$ , based on the kinematic analysis of the IPO chamber. Since both the valley and mountain creases of the structure are assumed to consistently maintain in arc shape and remain constant (Figs. 3d and 3e), the relationship between the radius and corresponding central angle of the creases can be derived as

$$\left\{ \begin{array}{l} R_m \gamma_m = R_{m0} \gamma_{m0} \\ R_m \sin\left(\frac{\gamma_m}{2}\right) = \frac{H_p}{2} \\ R_v \gamma_v = H_{p0} \\ R_v \sin\left(\frac{\gamma_v}{2}\right) = \frac{H_p}{2} \end{array} \right., \quad (6)$$

where  $R_m$  and  $\gamma_m$  are the radius and central angle of the mountain creases, respectively,  $R_v$  and  $\gamma_v$  are the radius and central angle of valley creases, respectively. Parameters ending with the subscript '0' represent the corresponding parameters in the initial state.

The dihedral angles of the creases on the equatorial plane of the structure are further analyzed (Fig. 3c). By establishing a Cartesian coordinate system on this plane, the vector analysis method can be adopted to solve the corresponding angle values in triangle OPQ. The dihedral angle of the mountain creases and valley creases can be derived as

$$\left\{ \begin{array}{l} \beta_m = 2 \arccos \left( \frac{\vec{OP} \cdot (\vec{OP} - \vec{OQ})}{\|\vec{OP}\| \cdot \|\vec{OP} - \vec{OQ}\|} \right) \\ \beta_v = \beta_m + \beta_{v0} \end{array} \right., \quad (7)$$

where the magnitudes of the vectors  $\vec{OP}$ ,  $\vec{OQ}$ , as shown in Figs. 3d and 3e, can be derived as

$$\left\{ \begin{array}{l} \|\vec{OP}\| = MP - MO = R_m \left( 1 - \cos \frac{\gamma_m}{2} \right) \\ \|\vec{OQ}\| = VQ - VO = R_v \left( 1 - \cos \frac{\gamma_v}{2} \right) \end{array} \right., \quad (8)$$

and the vectors  $\vec{OP}$ ,  $\vec{OQ}$  can be expressed as

$$\begin{cases} \vec{OP} = \left( 0, R_m \left( 1 - \cos \left( \frac{\gamma_m}{2} \right) \right) \right) \\ \vec{OQ} = \left( \|\vec{OQ}\| \sin \angle POQ, \|\vec{OQ}\| \cos \angle POQ \right) \end{cases}, \quad (9)$$

The bending moments around the creases,  $M_m$  and  $M_v$ , are determined by angular displacements  $\Delta\beta_m$  and  $\Delta\beta_v$ , and the corresponding lengths of the folding regions  $l_m$  and  $l_v$ . The facets of the curved convergent folding units, which are assumed to be perpendicular to the related creases during deformation, are defined in the initial state (Fig. 3b). The width of the facets of the mountain folding units  $L_m$  at an angle  $\theta_m$  with the horizontal is defined as the length of the line segment where the plane passing through the radius and perpendicular to the pleat intersects the pleat. The width of the facets of the valley folding units  $L_v$  at a distance  $h$  from the equatorial plane is defined as the length of the line segment where the plane passing through the radius and perpendicular to the pleat intersects the pleat. The length of the folding region of the mountain creases and valley creases,  $l_m$  and  $l_v$ , which are treated to be proportional to the width of their facets and can be represented as

$$\begin{cases} l_m = qL_m = qR_{m0} \left( 1 - \frac{\cos(\frac{\gamma_{m0}}{2})}{\cos(\frac{\theta_m}{\gamma_m} \gamma_{m0})} \right) \\ l_v = qL_v = q \left( \sqrt{R_{v0}^2 - \left( \frac{\theta_v}{\gamma_v} H_0 \right)^2} - R_{v0} \cos \left( \frac{\gamma_{v0}}{2} \right) \right) \end{cases}, \quad (10)$$

where  $L_m$  and  $L_v$  are the width of the facets of mountain and valley creases, respectively.  $\theta_m$  ( $\theta_m \leq \gamma_m/2$ ) and  $\theta_v$  ( $\theta_v \leq \gamma_v/2$ ) are the equatorial section angles, respectively.  $\gamma_m$  and  $\gamma_v$  are the central angles of the mountain creases and valley creases, respectively.  $q$  is the coefficient that indicates the length of the folding region and can be calibrated experimentally.

According to the SSF principle, quasi-static analysis of the folding units is treated as a cantilever beam being bent at the bending region  $l_m$  and  $l_v$ . Together with the folding angles derived in Eq. (7), the folding moments generated by single mountain crease or valley crease can be derived as

$$\begin{cases} M_m = \int dM_m = \int d \frac{EI_m}{\rho_m} = \int d \frac{EI_m \Delta\beta_m}{2l_m} \\ M_v = \int dM_v = \int d \frac{EI_v}{\rho_v} = \int d \frac{EI_v \Delta\beta_v}{2l_v} \end{cases}, \quad (11)$$

where  $I_m = \frac{t_p^3 R_m d\theta_m}{12}$  and  $I_v = \frac{t_p^3 R_v d\theta_v}{12}$  are the moments of inertia of the cross-section of the mountain crease and valley crease, respectively. For curved convergent creases, since the width of the facets approaching zero near the ends of the creases, effective unfolding motions cannot be achieved. Therefore, the foldable parts of the pleats are considered to exist only in the middle parts of the creases. This is also verified by preliminary finite element analysis (FEA) results (Figs. 3d and 3e). Abaqus/Standard was used for the FEA of the quasi-static deformations of the IPO chamber. The simulation parameters of the IPO chamber are presented in Table 2. Detailed meshing methods can be referred to Supplementary S3. The bottom end-face of the chamber are fully constrained, while the upper end-face employs point-plane coupling to restrict its self deformation, simulating the adhesive bonding constraints between the end-face and high-stiffness components in practical applications. By substituting Eqs. (7) and (10) into Eq. (11), the moment generated by individual mountain crease or valley crease can be derived as

$$\begin{cases} M_m = D_m \Delta\beta_m = D_m \beta_m \\ M_v = D_v \Delta\beta_v = D_v \beta_v \end{cases}, \quad (12)$$

where  $D_m$  and  $D_v$  are coefficients that are independent of the deformation state, and can be expressed as

$$\begin{cases} D_m = \frac{Et_p^2 \gamma_{m0}}{12q} \int_0^{\frac{K}{2}} \frac{1}{1 - \cos \left( \frac{\gamma_{m0}}{2} \right) / \cos(k\gamma_{m0})} dk \\ D_v = \frac{Et_p^3 H_{p0}}{12q R_{v0}} \int_0^{\frac{K}{2}} \frac{1}{\sqrt{1 - \left( 2k \sin \left( \frac{\gamma_{v0}}{2} \right) \right)^2} - \cos \left( \frac{\gamma_{v0}}{2} \right)} dk \end{cases}. \quad (13)$$

where  $K$  represents the ratio of the length of the foldable part of the creases to the total length of the creases.

By substituting the Eqs. (6) and (12) into Eq. (5), the pseudo resisting force of IPO in vertical direction can be derived as

$$F_{PR}(\gamma_m, \gamma_v) = u_p \beta_m (D_m + D_v) \left( \frac{\partial \beta_m}{\partial \gamma_m} \cdot \frac{1}{\frac{dH_p}{d\gamma_m}} + \frac{\partial \beta_v}{\partial \gamma_v} \cdot \frac{1}{\frac{dH_p}{d\gamma_v}} \right). \quad (14)$$

Together with the relationship among  $\beta_m$ ,  $\gamma_m$  and  $\gamma_v$  have been derived in Eqs. (7), the differential parts of the equation can be obtained. Thus, the relation between the pseudo resisting force and the displacement of IPO chamber can be estimated.

As for the active force of the IPO chamber, unlike the capacity of EYO chamber that has been verified to be almost linearly related to its height, the capacity of IPO chamber exhibits a distinct non-linear relationship with its height. According to Eq. (2), the active force of IPO chamber can be derived as

$$F_{PA} = P_p \frac{dV_p}{dH_p} = P_p S_p, \quad (15)$$

where  $P_p$  is the relative pressure in the IPO chamber,  $V_p$  is the capacity of IPO chamber.  $S_p = \frac{dV_p}{dH_p}$  is the equivalent area of IPO chamber which varies at different heights and can be calibrated using curve fitting experimentally.

Although we have derived the quasi-static model of the IPO chamber by adopting the reduced-order method, the modeling methodology based on a set of assumptions may exhibit certain limitations in practical applications. In contrast to the EYO chamber that deformed almost in the same way whether passively compressed or actively deflated, deformation of the IPO chamber when passively compressed is quite different from the actively inflated situation and nearly unpredictable. Here, we analyze the resisting force of IPO chamber based on the predictable unfolding motion of the creases when actively inflated. Therefore, for situations when the IPO chamber is compressed without sufficiently pressurized (the pressure value reaches the specified value when the cavity is pressurized to the target position under load-free condition), the model might struggle to provide an accurate analysis.

#### 4. Design and fabrication of NDO actuator

To validate the NDO concept and the quasi-static models, a prototype of the NDO actuator was designed and fabricated as shown in Fig. 4.

In designing the dimensions for the two chambers, a critical issue that should be addressed is the potential structural interference due to the radial expansion of the IPO chamber and the minimum radial dimension of the internal space within the EYO chamber as the actuator contracts. As shown in Fig. 4a, the maximum external contour of the chamber is confined within a cylindrical boundary during the radial expansion of the IPO chamber. This boundary is defined by the diameter of the circumscribed circle of the equatorial layer cross-section and the overall height of the chamber. Thus, the maximum radial diameter  $D_{max}$  during the unfolding process can be defined as the diameter of a circle. The circumference of the circle is equal to that of the contour of the shape intersected by the equatorial plane. The minimum radial

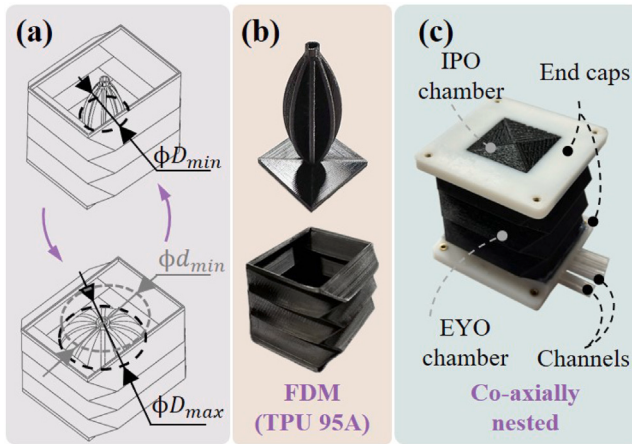


**Fig. 4.** Design and fabrication of the NDO actuator. (a) The minimum radial dimension of the EYO chamber is determined by the largest radial magnitude of the IPO chamber during expansion. (b) The prototypes of the origami chambers are made of TPU 95A by FDM and coaxially nested with the help of the end caps that made of resin by SLA to form (c) the NDO actuator.

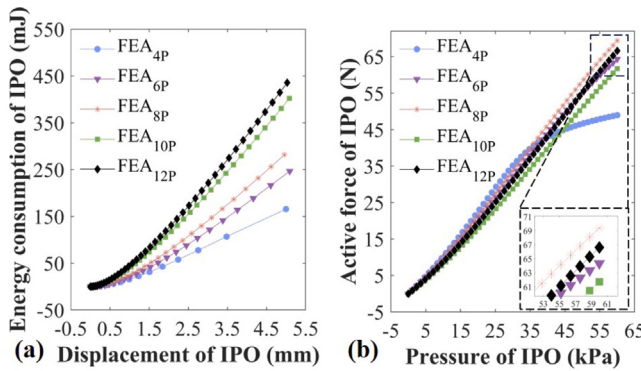


**Fig. 5.** FEA comparison of IPO chambers with different pleats. (a) Energy consumption under various displacement. (b) Output force in initial length under various pressure.

dimension  $d_{\min}$  of the EYO chamber is determined by the diameter of the inscribed circle of the end face shape.

For the EYO chamber, combined with the matching requirements, the simplest typical Yoshimura chamber with a quadrilateral end face was chosen. The detailed design parameters are shown in Table 1.

As for the IPO chamber, the number of pleats is related to the initial central angle of the arc. To ensure the maximum contraction of the IPO chamber, the width of the facets should be sufficient to compensate for the length of the connecting plate required when the valley folds transitions from a straight line to a semicircular arc. With the same initial height, a smaller central angle of the arc results in a shorter length provided by the facets. Thus, a decreasing number of pleats will result in an increasing central angle of the mountain crease, and their relationship can be derived as

$$\left\{ \begin{array}{l} R_{m0}^2 - \left( R_{m0} - \frac{\pi \left( \frac{H_{P0}}{\pi} + \frac{w}{2 \sin(\pi/u_p)} \right)}{u_p} \right)^2 = \left( \frac{H_{P0}}{2} \right)^2 \\ \gamma_{m0} = 2 \arcsin \left( \frac{H_{P0}}{2R_{m0}} \right) \end{array} \right. . \quad (16)$$

**Table 2**  
Design parameters of the IPO chamber.

Geometry parameter	Value
Thickness $t_p$	0.6 mm
Height $H_{P0}$	60 mm
Width of the pleat $w$	2.2 mm
Angle of the mountain crease arc $\gamma_{m0}$	70°
Angle of the valley crease arc $\gamma_{v0}$	0°
Angle of the mountain crease $\beta_{m0}$	0°
Angle of the valley crease $\beta_{v0}$	45°

The complete derivation of the formula can be referred to Supplementary S2. To compare the energy consumption and output force performance of IPO chambers with various numbers of pleats, FEA was conducted in Abaqus/Standard in two situations (see Supplementary S3): (1) Inflate the chamber to contract in load-free state (Fig. 5a); (2) Inflate the chamber in initial length with fixed ends (Fig. 5b). The simulation result indicates that the 8-pleats IPO chamber costs relatively low energy among the tested chambers (4, 6, 8, 10, 12 pleats) when contracts and generates the greatest output force. Practical manufacturing has confirmed that IPO chambers with fewer pleats results in a larger overhang angle at the actuator's end, leading to manufacturing defects (see Supplementary S3). Taking these facts, an IPO chamber with 8 pleats with an initial central angle of 70° was selected. The specific parameters are presented in Table 2.

After completing the design of the two chambers, we further utilized fused deposition modeling (FDM) 3D printing technology, with the high-stiffness Thermoplastic Polyurethane (TPU) material (TPU-95A, eSUN), to fabricate the chambers efficiently and reliably (Fig. 4b). The thicknesses of the IPO and EYO chambers are 0.6 mm and 0.75 mm, respectively, which ensures airtightness, smooth folding motion, and restricts the energy consumed by the deformation of the origami structure. The printing path in each layer of the chambers was designed to be continuous to avoid nozzle skipping that could induce filament retraction and result in porous printing walls [24]. The printing path width is 0.38 mm, which is between half the membrane thickness and one membrane thickness, leading to partial overlap between the two printing paths in each layer and ensuring the airtightness of the structures. Moreover, the membranes were printed without supporting structures to prevent discontinuous paths and potential damage to the membranes during removal. In addition to the two soft chambers, two end caps, fabricated from photosensitive resin using stereolithography apparatus (SLA), were designed to enclose the origami structures at both ends, forming the NDO actuator (Fig. 4c). Channels and air inlets for both chambers are integrated into the end caps, contributing to a more compact design.

## 5. Experiment validation

In this section, we will experimentally investigate and verify the effectiveness and the quasi-static model of the NDO actuator, which includes the resisting and active forces of the two chambers. The coefficients  $n$ ,  $m$ ,  $q$  and  $K$  will be calibrated to derive the specific model for the resisting force. The equivalent areas of both the chambers, expressed as the change in volume with height, will be obtained experimentally.

### 5.1. Performance of the EYO chamber

The experiments on the EYO chamber were conducted using a pneumatic setup, which includes a pneumatic system (Fig. 6a) and an experimental platform (Fig. 6b). The pneumatic system is designed based on the Pump-valve method through a microcontroller (STM32f103c8t6, ST Inc.) to regulate two solenoid valves for each pneumatic channel. Corresponding displacement and force data is measured by a laser

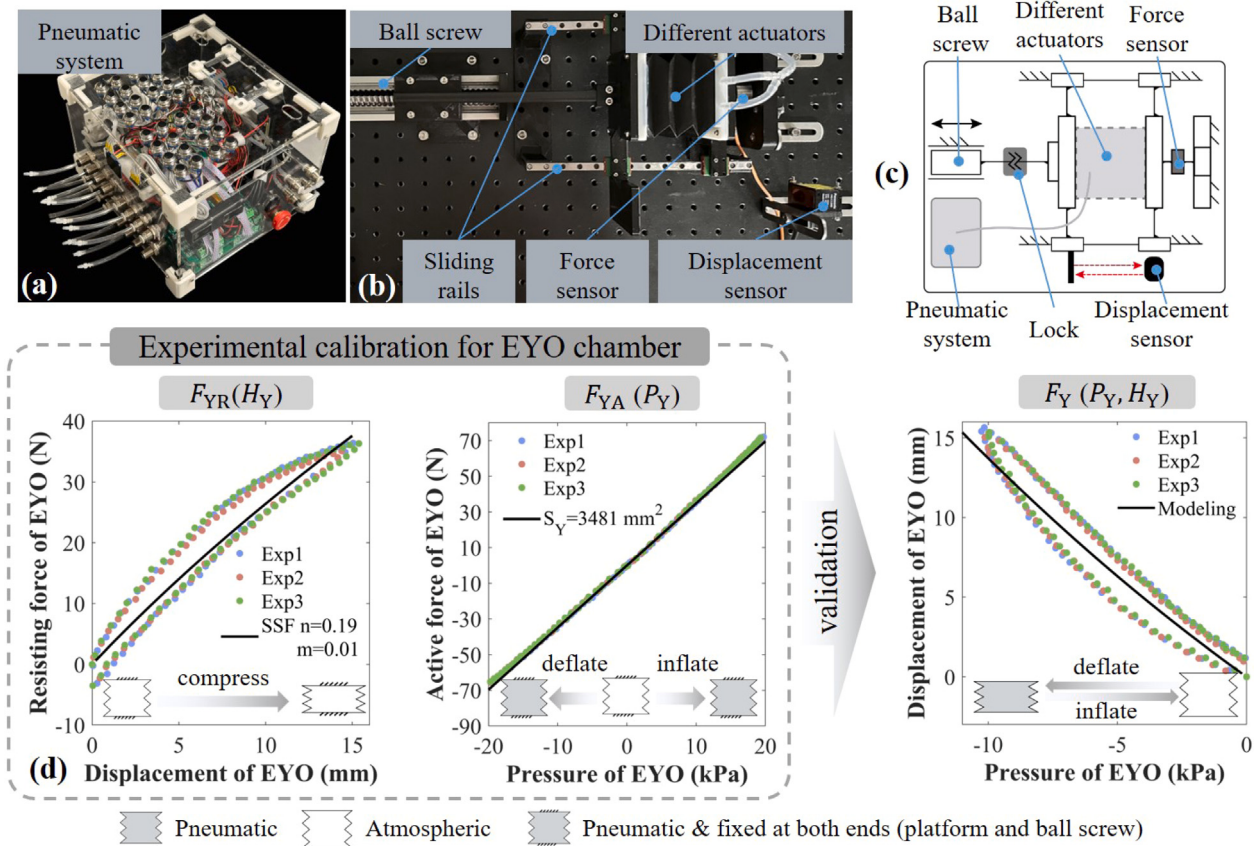


**Fig. 6.** Characteristics of the EYO chamber. Pneumatic experimental setup for the actuators includes (a) the pneumatic actuation system and (b) pneumatic experimental platform for exploring the mechanical properties of three actuators. (c) Schematic representation of the pneumatic setup. (d) Test results of the resisting force. (e) Test results of the active force. (f) Displacement and pressure of EYO in load-free condition was measured to validate the quasi-static model.

sensor (HG-C1100, Panasonic Inc.) and 1-DOF force sensors (DYMH-103, 0–10 kg and 0–50 kg, DAYSENSOR Inc.). The schematic diagram of this experimental setup is shown in Fig. 6c, a single-chamber EYO actuator was installed on this setup to explore its mechanical properties and payload performance.

We first conducted the resisting force test on the EYO chamber. During this test, the single-chamber EYO actuator was compressed and released intermittently using a ball screw, with its chamber connected to the atmosphere. The compression speed was set slow (0.3 mm/s) to minimize the effects of inertial motion. The displacement and output force data were recorded and shown in Fig. 6d. The coefficients  $n$  and  $m$  calibrated from the test were found to be  $n = 0.19$ ,  $m = 0.01$ , respectively. The modeling results and the median values of the measured data show good agreement.

Then, to investigate the active force, the EYO actuator was repeatedly deflated and inflated by the pneumatic system at initial length. The data for pressure and force were recorded (Fig. 6e). The equivalent area of the EYO chamber  $S_Y$ , derived in Eq. (4), was obtained by calculating the slope of the fitting line, resulting in  $S_Y = 3481 \text{ mm}^2$ . The well-fitting result further validates the strong linear relationship between the relative pressure and the active force of the EYO chamber.

Moreover, the quasi-static model of the EYO chamber,  $F_Y = F_{YR}(H_Y) + F_{YA}(P_Y)$ , was tested and verified. An experiment was conducted to validate the relationship between relative pressure and displacement of the EYO actuator in the contraction and load-free condition. The experimental data and modeling results are shown in Fig. 6f. The good agreement between the modeling results and the median values of the measured data effectively validates the quasi-static model of the EYO chamber. Processes of characteristics of the EYO chamber can be referred to Supplementary Movie S1.

So far, we have evaluated the basic performance of the EYO chamber and calibrated coefficients of the quasi-static model based on the test results. Next, we will carry out analogous experiments and analysis on the IPO chamber.

## 5.2. Performance of the IPO chamber

The performance of the IPO chamber was tested on both the mentioned pneumatic setup and the hydraulic setup for measuring the volume change. In the hydraulic setup, the pneumatic system was replaced by a syringe filled with water, which served as the fluid supply for the actuators (Fig. 7a). The syringe's linear motion was actuated by a ball screw at a low speed of 0.3 mm/s, and the displacement was measured using a laser sensor (HG-C1200, Panasonic Inc.). Fluid pressure was monitored with a pressure sensor (XGZP6857 A, CFsensor Inc.). The schematic diagram of this experimental setup is shown in Fig. 7b. A single-chamber IPO actuator was fabricated for the subsequent experiments.

The equivalent area and coefficients of resisting force for the IPO chamber were calibrated simultaneously in the hydraulic experimental setup, based on the principle of virtual work as

$$F_{PR} = P_S S_S \frac{dH_S}{dH_P} \quad (17)$$

where  $S_S = \pi \cdot 12.1^2 \text{ mm}^2$  is the sectional area of the syringe.  $P_S$  is the pressure of the liquid inside the syringe and actuator.  $dH_S$  is the displacement of the syringe. The experiment was conducted in a load-free condition by slowly compressing the syringe, which expelled water into the IPO chamber to induce contraction. Compared to using air as the experimental medium, the nearly incompressible water results

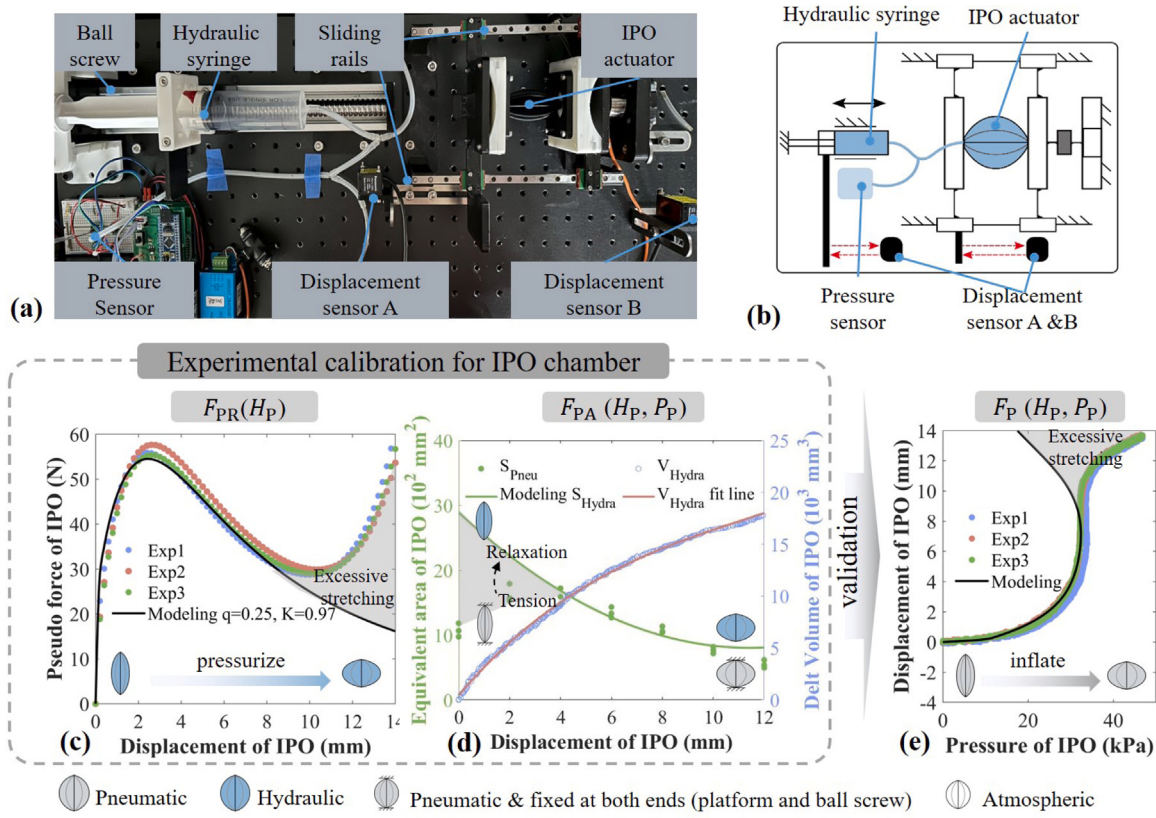


**Fig. 7.** Characteristics of the IPO chamber. (a) Hydraulic experimental setup to test the resisting force of the IPO chamber. (b) Schematic representation of the hydraulic setup. (c) Test results of the resisting force. (d) Active force testing for calibrating the equivalent area at different displacements. (e) Displacement and pressure of IPO in load-free condition is measured to validate the quasi-static model.

in negligible energy loss during chamber pressurization and provide a directly measured of the volume change of the IPO chamber. The experimental and modeling results of the resisting force are depicted in Fig. 7c.

The coefficients  $K$  and  $q$  in Eq. (12), calibrated by the test, were found to be  $K = 0.97$ ,  $q = 0.25$ . The modeling of the resisting force attributes the energy cost during deformation to the unfolding motion of the creases. This ensures that the quasi-static model aligns substantially with the experimental results when the material exhibits negligible stretch. However, in actual conditions, once the creases are almost unfolded at the displacement around 8 mm, the contraction motion of the actuator will inevitably generate material in-plane stretching, which results in a significant difference from the modeling results at relatively large displacements.

The equivalent area of IPO chamber is another key model parameter affecting its active force, which is derived from the Eq. (15) as the slope of the displacement-volume fitting curve in the hydraulic experiment. The volume change and relative displacement of the IPO chamber during the hydraulic test are depicted in Fig. 7d. The resulting equation is  $S_p = 16(H_{P0} - H_p)^2 - 365.5(H_{P0} - H_p) + 2889.1$  ( $\text{mm}^2$ ). We further tested the equivalent area in different displacements in the pneumatic setup. The IPO actuator was inflated pneumatically to specified displacements, then both ends of the actuator was fixed and further pressurized by increments of 15 kPa. The equivalent areas, in the pneumatic experiment, was obtained by calculating the slope of the fitting curves of the axial force and the pressure during the additional pressurization stage. The modeling result derived from volume change showed significant differences from the pneumatic experiment in the low-pressure stage. The primary reason is the substantial difference in the unfolding extent between the two tests. During the hydraulic experiment, the actuator was tested in a load-free condition, and the pressure required to reach small displacements was relatively low,

resulting in only minor unfolding of the creases. However, in the pneumatic experiment, the pressure was increased by at least 15 kPa increments, which led to more unfolding of the creases and a larger volume at the same displacement. When the pressure exceeded 35 kPa, the pressure increments tended to produce less volume change, which made the model consistent with the experiment at the higher-pressure stage.

Based on the above experimental results, we have calibrated the quasi-static model of the IPO chamber,  $F_p = F_{PR}(H_p) + F_{PA}(P_p, H_p)$ . Fig. 7e displays these experimental results which exhibit a high degree of alignment with the experimental observations during the phase of minor displacement. Once the creases have been adequately unfolded to generate larger displacements, the resistance encountered primarily arises from the substantial in-plane stretching of the facets. As mentioned earlier, the quasi-static model is derived based on the unfolding motion with negligible in-plane stretching, therefore, once the displacement of the IPO chamber exceeded 8 mm (Fig. 7e), it constitutes a domain that falls outside the predictive scope of the present model. This results in significant errors in the subsequent portions of the displacement range. Processes of characteristics of IPO chamber can be referred to Supplementary Movie S2.

### 5.3. Performance of the NDO actuator

Having completed the testing and analysis of the basic performance of the single-chamber EYO and IPO actuators respectively, this section will focus on the performance of the NDO actuator. This includes the quasi-static model of the NDO actuator, derived in Eq. (1), and the NDO structure's capability to provide bidirectional payload enhancement through compounding pressure actuation.

We first validate the quasi-static model by examining the relationship between the relative pressure and displacement of the NDO

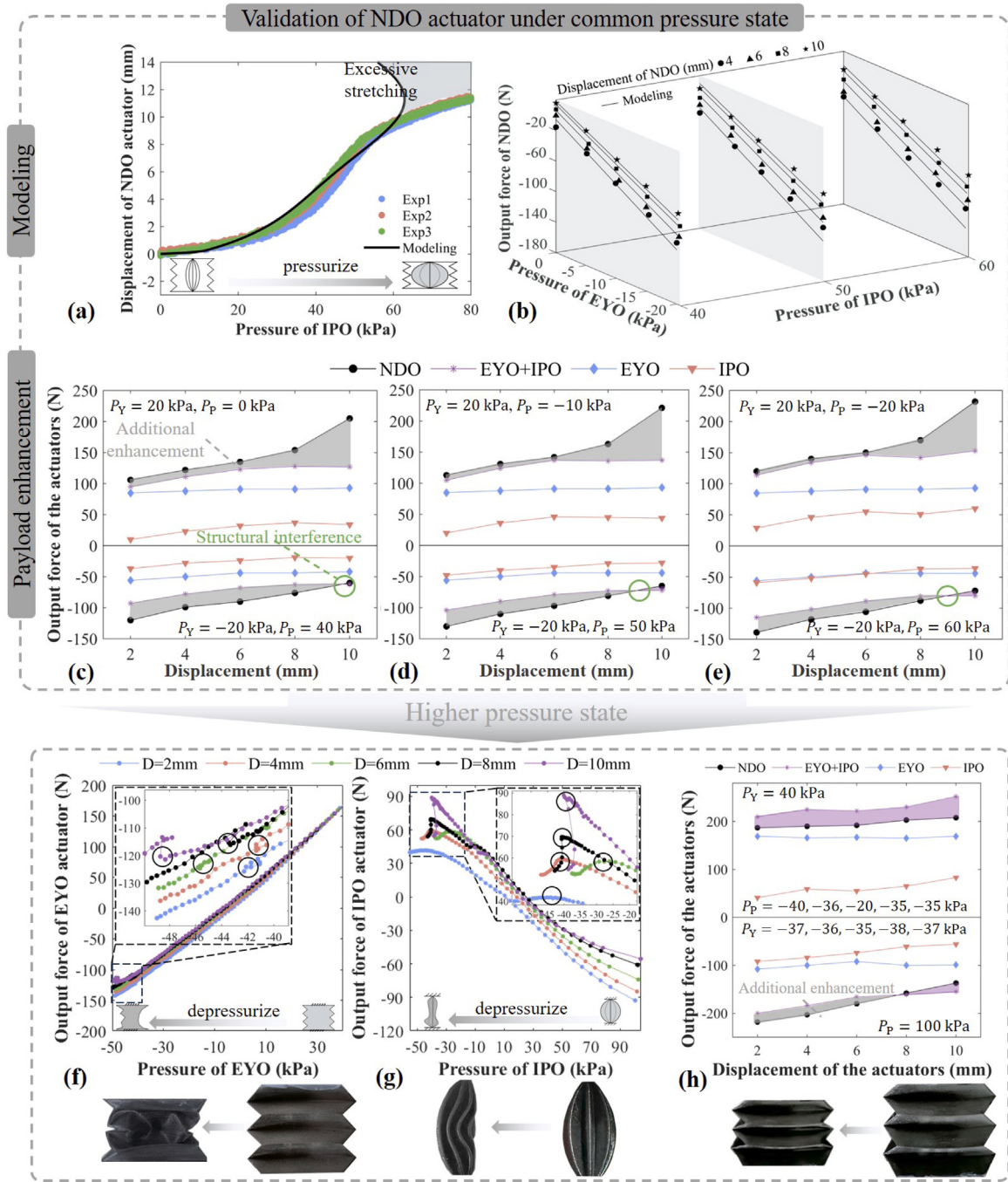


**Fig. 8.** Characteristics of NDO actuator. (a) Pressure-Displacement validation in the load-free condition of the quasi-static model of NDO actuator. (b) Pressure-Force validation in different displacements and different pressure in the IPO chamber of the quasi-static model of NDO actuator in the contraction direction. (c-e) Validation of the payload enhancement of the NDO structure at low pressure ranges and different displacements, compared with the payload generated by single-chamber actuators or the sum of both actuators. (f) and (g) Output forces of the EYO and IPO chamber were recorded over large range of pressures to investigate the buckling pressure values at different displacements. (h) Validation of the payload enhancement of the NDO structure under higher pressure state.

actuator. The test followed the procedure of the EYO validation test, with the EYO chamber connected to the atmosphere and the IPO chamber connected to the pneumatic system. The experimental and modeling results are presented in Fig. 8a, showing obvious consistency at smaller displacements. The model shows discrepancies when the displacement exceeds 8 mm, due to the lower stiffness of the IPO chamber predicted by the model under excessive deformation. Processes of characteristics of the NDO actuator can be referred to Supplementary Movie S3.

Next, the model was validated by assessing the relationship between relative pressure and output force of the NDO actuator. The IPO chamber pressure was set to 40, 50 and 60 kPa, while the EYO chamber pressure was adjusted to five equidistant values from -20 to 0 kPa. The test was conducted at displacements of 4, 6, 8 and 10 mm. The results are shown in Fig. 8b. The model's predictions are consistent under lower relative pressure and smaller displacement. However, as the relative pressure and displacement increase, the model's underestimation of the material's in-plane stretching leads to an overestimation of the predicted output force.

Then the NDO structure's effectiveness in enhancing bidirectional payload performance under common pressure ranges was verified (lower pressures that cause less in-plane stretch). The output force of the NDO actuator and the independent actuators was tested under various displacements and pressures. In the elongation state, the EYO chamber pressure was  $P_Y = 20$  kPa and the IPO chamber pressure was  $P_p = 0, -10$  and -20 kPa. In the contraction state, the EYO chamber pressure was  $P_Y = -20$  kPa and the pressure of IPO chamber was  $P_p = 40, 50$  and 60 kPa. The experimental results are shown in Figs. 8c–e. Compared to the sum of two independent actuators, the NDO actuator's output force showed enhancement at nearly all tested displacements and pressure combinations. The average enhancement of the contraction force reached 101.7% compared to the EYO actuator and 21.2% compared to the sum of the independent actuators. The average enhancement of the elongation force reached 70.5% compared to the EYO actuator and 19.7% compared to the sum of two independent actuators.

The bidirectional payload enhancement of the NDO structure under higher pressure state was further tested. We first tested the output forces of both chambers under high pressure at different displacements to identify the pressure limits before irregular deformation (see Supplementary Movie S4). The results are depicted in Figs. 8f and 8g. The EYO chamber's buckling pressure ranges from -50 to -40 kPa, leading to significant deformation and a decrease in axial force. Buckling in the EYO membrane causes indeterminacy in motion direction and uncontrolled vibrations, compromising precision and reliability. The IPO chamber's distortion pressure ranges from -45 to -30 kPa, resulting in macroscopic bending and a reduction in output force.

The NDO structure was then tested with pressure near the buckling pressure. The EYO chamber's pressure was set 5 kPa below the buckling pressure, and the IPO chamber's relative pressure was set 5 kPa below the distortion pressure. The positive pressures were 40 kPa for the EYO chamber and 100 kPa for the IPO chamber. The results in Fig. 8h show that the NDO structure still enhances payload in the contraction direction under higher pressure states. In the elongation direction, although the NDO structure enhances payload, the IPO chamber is prone to excessive deformation, limiting additional enhancement. The average enhancement of the contraction force reached 79.4% compared to the EYO actuator and 9.3% compared to the sum of the independent actuators. The average enhancement of the elongation force reached 17.2% compared to the EYO actuator.

In addition to experimental validation of the NDO's effectiveness, we further conducted FEA to investigate the interaction mechanism between the two chambers. The material properties of the TPU95A was obtained with uniaxial tensile tests of the Dogbone specimens printed in two orthogonal directions (Supplementary Material S1).

Since the NDO actuator incorporates two chambers coaxially nested, the coupling effect between these chambers results in varied output

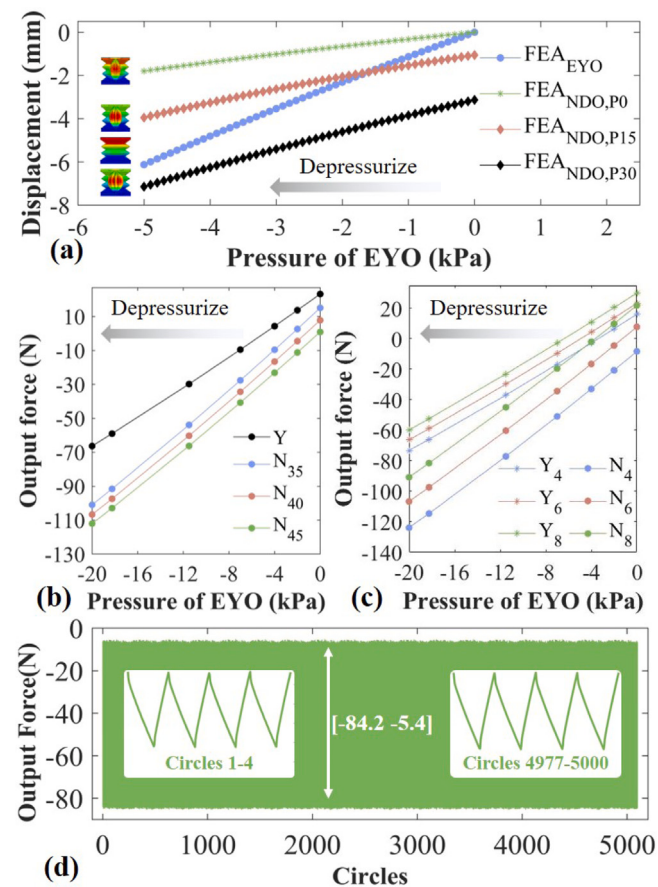


**Fig. 9.** Operational mechanism of the NDO actuator. (a) Displacement comparison of the independent EYO actuator and NDO actuator with IPO chamber under different pressures. (b) Output force enhancement with different pressure IPO pressure ( $P_p = 35, 40, 45$  kPa). (c) Output force enhancement compared to EYO actuator in different displacements (displacement = 4, 6, 8 mm). (d) An endurance test of the NDO actuator with periodic contact for around 5000 circles.

performance and stress state under different combinations of displacements and pressures. For example, when applying the EYO chamber with moderate pressure (-5 kPa), the EYO chamber is able to reach a displacement about 6 mm (Fig. 6f). In comparison, the PO chamber only generates negligible displacement (Fig. 7e). Such a displacement disparity causes the presence of the IPO chamber to impede, rather than facilitate the motion of the EYO chamber under low pressure situation. Fig. 9a shows FEA result of the displacements generated by individual EYO actuator, or NDO actuator with IPO chamber in various pressure (0, 15 and 30 kPa, refer to Supplementary S4 for detailed FEA process). The result indicates that the desired improvement is able to maintain the throughout the motion only when the pressure difference is sufficient to generate a displacement comparable to that of the independently actuated EYO actuator. Consequently, a pre-pressurization of the IPO chamber becomes necessary in this scenario to achieve the desired displacement enhancement.

Once the payload enhancement is ensured, the contribution of the IPO chamber is able to improve the output force generated by the pressure difference  $P_p - P_Y$ . We stimulated EYO and NDO actuator with different  $P_p$  in the displacement of 6 mm. As shown in Fig. 9b, introduction of IPO chamber acts to lower the intersection points of all segments with  $P_Y = 0$  while simultaneously increasing their slopes. Subsequent FEA further verified the efficacy of the IPO chamber in delivering a dual performance enhancement to the NDO actuator under different displacements (Fig. 9c).

**Table 3**  
Performance comparison of linear SPAs in existing literature.

Research deformation during inflated	Dimension (mm)	Pressure range (kPa)	Axial force (N) (contraction, elongation)
[11] Elongation	$\phi 31 \times 52$	(−60, 96)	(−50, 72)
[15] Contraction	530 × 210*(Thin thickness)	(0, 50)	(−200, 0)
[28] Elongation	$\phi 40 \times 40$	(−52, 160)	(−60, 192)
[33] Elongation	46 × 16 × 150	(−90, 0)	(−428, 0)
[36] Elongation	$\phi 34 \times 131$	(0, 50)	(0, 22)
[46] Contraction	$\phi 30 \times 260$	(0, 100)	(−270, 0)
[72] Elongation	$\phi 48.8 \times 6$	(0, 120)	(0, 149.7)
[73] Elongation	84 × 19 × 175	(0, 100)	(0, 112)
This work	75 × 75 × 73.5	EYO(−38, 40) & IPO(−40, 100)	(−218, 208)
Elongation & Contraction			

Although the NDO structure can still enhance the output of the single-chamber actuator when contact happens with large displacement (Fig. S6f), analysis of the output behavior remains challenging for the modeling method presented in this study. To validate the reliability of the NDO actuator when contact happens, we tested the NDO actuator in the situation that periodical contact happens (Supplementary Material S5). The testing result is depicted in Fig. 9d. The output force response proves highly repeatable over 5000 successive cycles without failure, well demonstrates the reliability of the actuator even with periodical contact between the chamber walls.

A comparison among the NDO actuator and other existing designs has been conducted. As shown in Table 3, unlike most SPAs that focus on unidirectional force output, the proposed coaxially-nested actuator is capable of achieving high bidirectional force output with compact design. Moreover, the NDO actuator also demonstrates superiority in payload performance in opposite directions over SPAs that emphasize bidirectional force output.

The testing results validating the analytical modeling of the NDO structure together with its robust bidirectional payload capability. In the subsequent section, we will utilize this NDO actuator as a soft actuation core to design a robotic system and apply it in practical applications.

## 6. NDO gripper with enhanced stretching and gripping force

To better demonstrate the enhancement in bidirectional payload capabilities, two soft grippers were constructed, one with EYO actuator and the other with NDO actuator, as shown in Fig. 10a. When the actuators elongate, the ends of the gripper move apart, and get close when the actuators contract. The gripping space of the gripper ranges from 0 to 57 mm, which is similar to the size of the cross-section of the gripper. The compact design and bidirectional output facilitate the gripper's ability to separate obstacles, simultaneously pass through narrow openings, and accomplish gripping task.

The stretching and gripping forces of the gripper were measured to quantify the force enhancement. The experimental setup is able to transfer these forces to a force sensor attached to the gripper's end, as shown in Fig. 10b. By adjusting the position of the limiters fixed on either side of the force sensor, we can measure the gripper's output force at various gripping positions. Based on this setup, we conducted tests at four different positions ( $L = 15, 25, 35, 45$  mm), using either the EYO or the NDO actuator as the actuation device. The results from the stretching and gripping tests are presented in Fig. 10c. For the NDO actuator, the IPO chamber's internal pressure was maintained at 100 kPa during gripping, and at 0 kPa during stretching. The pressure in the EYO chambers for both actuators was adjusted uniformly from −45 to 40 kPa. The data revealed that, in the gripping mode, the average increases in force were 3.5, 6.8, 4.4, and 16.9 N, respectively, and in the stretching mode, the average increases were 14.3, 13.9, 17.4, and 9.2 N, respectively. This demonstrates that the NDO actuator consistently enhanced the gripper's output forces across all tested positions and modes.

The gripper was further tested and applied in a simulated narrow and confined environment (Fig. 10d). A simple soft robotic manipulator, equipped with two single-chamber EYO actuators for vertical motion, was constructed. The NDO actuator, which is only 128 g, is used to retrieve a 2 kg cylinder weight with a 35 mm diameter from a 30 mm gap between two 2.3 kg bricks placed on 100 Cw sandpapers, which provided significant friction resistance (Figs. 10e and 10f and Supplementary Movie S5). The soft manipulator was designed to first use its stretching force to separate the bricks and create a sufficient gap (stage (ii)), then grip the weight's smooth sides (stage (iv)), and lift it out of the narrow environment (stage (v)). The EYO gripper could only separate the bricks but failed to grip the weight with inner pressure at −32 kPa which causes buckling on the chamber (stage (iv)). In contrast, the NDO gripper successfully completed the task with 40 kPa in the IPO chamber and −26 kPa in its EYO chamber, without any irregular deformation (stage (iv)). This comparison demonstrates the advantages of the NDO structures, highlighting its potential for applications requiring large bidirectional payload output.

## 7. Conclusion

This paper presents the NDO structure which enables compounding pressure actuation for bidirectional output to overcome the inherent payload limitations in the direction actuated by negative pressure for linear SPAs. We constructed a linear NDO actuator by coaxially nested the EYO chamber and IPO chamber, according to the analysis on the structural symmetries and the motions of origami tubes. The two chambers conform all three symmetric conditions, performing opposite linear translation under same pressure state. The EYO chamber with parallel straight creases generates elongation under positive pressure, while the IPO chamber with curved convergent creases generates contraction under positive pressure.

To predict the mechanical behaviors and carry out parametric study on the structure, the quasi-static model of the NDO actuator is derived involving the resisting and active force. The resisting forces of the chambers are derived based on the SSF principle. Specifically, the resisting force of the IPO chamber, which consists of curved convergent creases, is derived by redefining the proportional relationship between the length of the folding region and the width of the facets, rather than the thickness of the facet in the SSF method.

The quasi-static model and the payload enhancement are validated with a 3D-printed NDO prototype. Within the validated pressure range of the model, the average enhancement of the contraction force of NDO actuator reaches 101.7% compared to the single-chamber EYO actuator and 21.2% compared to the sum of the single-chamber EYO and single-chamber IPO actuators. The average enhancement of the elongation force of NDO actuator reaches 70.5% compared to the EYO actuator and 19.7% compared to the sum of the single-chamber actuators. Although its enhancing effect attenuates under higher pressure conditions, it can still provide a favorable enhancement effect over EYO actuator. A compact gripper driven by the NDO actuator shows large stretching force and gripping force. The experimental results prove that

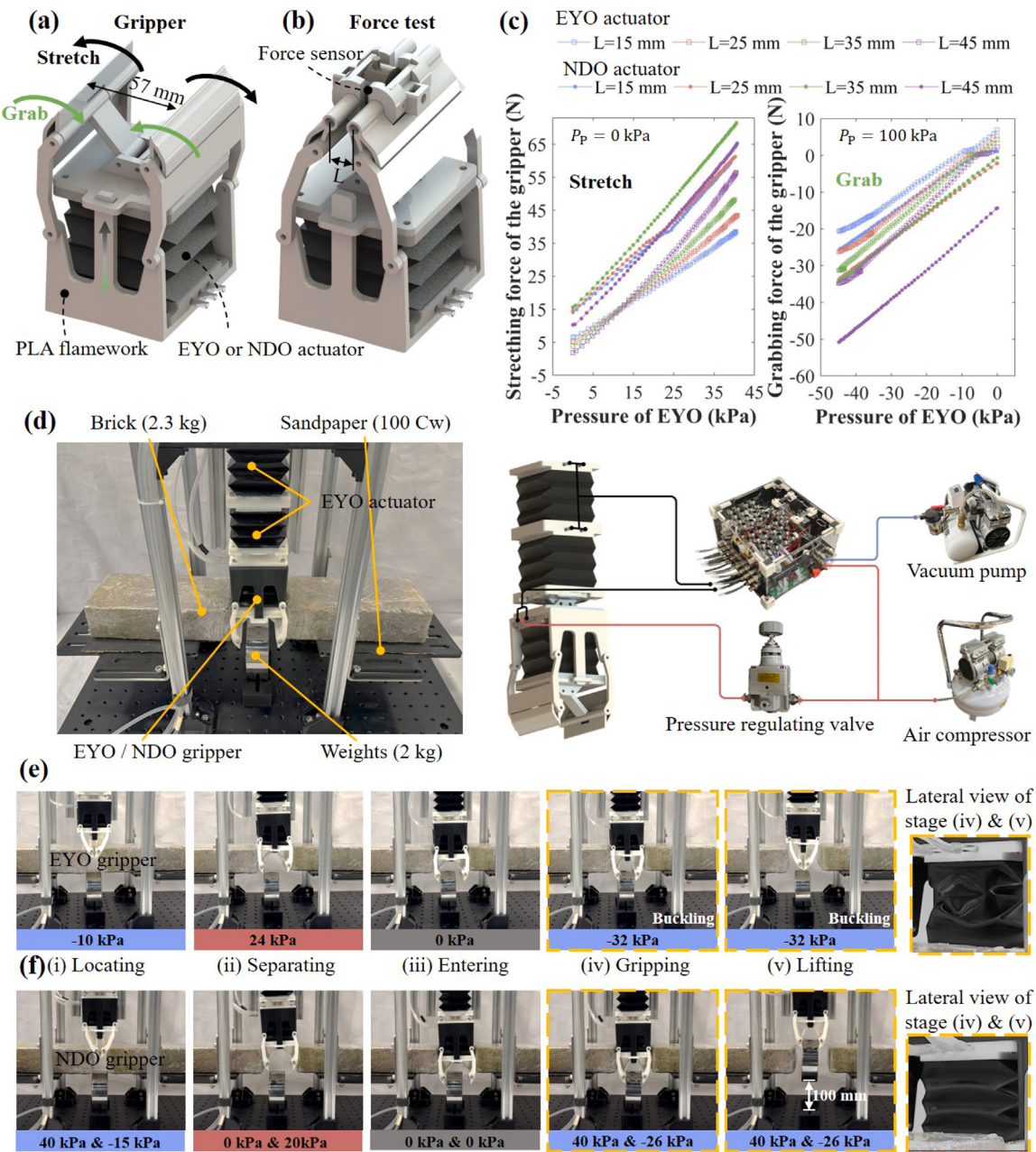


**Fig. 10.** NDO gripper and experiments on the mechanical performance. (a) An compact NDO gripper whose gripping range is similar to its cross-section was constructed. When the actuators elongate (contract), the gripper's end moves apart (close). (b) The experimental setup for measuring the stretching and gripping force of the gripper. (c) Experimental results of the stretching and gripping force of the gripper driven by the NDO actuator or the EYO actuator. (d) Experimental setup of the heavy object retrieval task in the confined narrow environment. (e) and (f) show tasks finished by EYO gripper and NDO gripper, respectively, with the compounding actuation pressure states of the NDO gripper represented as  $P_p \& P_Y$ .

the NDO actuator consistently enhanced the output force of the gripper across all the four tested clamping displacements in both gripping(17.4 N max) and stretching force (16.9 N max). By comparing with the gripper driven by the EYO actuator, the high bidirectional payload and stable performance of NDO actuator (128 g) enable the gripper to separate the 2.3 kg-each obstacle and pick up the 2 kg weight, accomplishing the heavy object retrieval task in the confined narrow environment. Hence, the practicality of the NDO approach is validated in soft robotic application.

Future research includes optimizing the NDO structure to achieve a greater range of motion, and optimizing the analysis of the origami units to account for in-plane stretching.

#### CRediT authorship contribution statement

**Xiaohuang Liu:** Writing – review & editing, Writing – original draft, Visualization, Methodology, Investigation, Formal analysis. **Zhonggui Fang:** Writing – review & editing, Writing – original draft, Supervision, Methodology, Investigation. **Shaowu Tang:** Writing – review & editing, Writing – original draft, Methodology, Formal analysis. **Fang Chen:** Methodology, Conceptualization. **Dihan Liu:** Conceptualization. **Sicong Liu:** Writing – review & editing, Supervision, Methodology, Investigation, Funding acquisition, Formal analysis, Conceptualization. **Juan Yi:** Supervision, Conceptualization. **Hongqiang Wang:** Supervision, Conceptualization. **Zheng Wang:** Supervision, Funding acquisition, Conceptualization. **Jian S. Dai:** Supervision, Funding acquisition.

## Declaration of competing interest

The authors declare that they have no known competing financial interests or personal relationships that could have appeared to influence the work reported in this paper.

## Acknowledgments

This work was partly supported by Natural Science Foundation of China Grant 52475302, the National Key R&D Program of China Grant 2022YFB4701200, Shenzhen Science and Technology Program Grant JCYJ20220530114615034 and Grant JCYJ20220818100417038, and Guangdong Provincial Key Laboratory of Intelligent Morphing Mechanisms and Adaptive Robotics Grant 2023B1212010005.

## Appendix A. Supplementary data

Supplementary material related to this article can be found online at <https://doi.org/10.1016/j.tws.2025.114187>.

## Data availability

All the data are included in the manuscript and supplementary files.

## References

- [1] B. Kalita, A. Leonessa, S.K. Dwivedy, A review on the development of pneumatic artificial muscle actuators: Force model and application, *Actuators* 11 (10) (2022) 288.
- [2] P. Polygerinos, Z. Wang, K.C. Galloway, R.J. Wood, C.J. Walsh, Soft robotic glove for combined assistance and at-home rehabilitation, *Robot. Auton. Syst.* 73 (2015) 135–143.
- [3] D. Duanmu, X. Wang, X. Li, Z. Wang, Y. Hu, Design of guided bending bellows actuators for soft hand function rehabilitation gloves, *Actuators* 11 (12) (2022) 346.
- [4] S. Liu, Y. Zhu, Z. Zhang, Z. Fang, J. Tan, J. Peng, C. Song, H.H. Asada, Z. Wang, Octariidae-inspired soft-robotic supernumerary flippers by fabric kirigami and origami, *IEEE/ASME Trans. Mechatronics* 26 (5) (2021) 2747–2757.
- [5] E.W. Hawkes, L.H. Blumenschein, J.D. Greer, A.M. Okamura, A soft robot that navigates its environment through growth, *Sci. Robot.* 2 (8) (2017) eaan3028.
- [6] E. Del Dottore, A. Mondini, N. Rowe, B. Mazzolai, A growing soft robot with climbing plant-inspired adaptive behaviors for navigation in unstructured environments, *Sci. Robot.* 9 (86) (2024) eadi5908.
- [7] M. Li, G. Wang, J. Wang, Y. Zheng, X. Jiao, Development of an inchworm-like soft pipe robot for detection, *Int. J. Mech. Sci.* 253 (2023) 108392.
- [8] J. Amend, N. Cheng, S. Fakhouri, B. Culley, Soft robotics commercialization: jamming grippers from research to product, *Soft Robot.* 3 (4) (2016) 213–222.
- [9] Y. Fei, J. Wang, W. Pang, A novel fabric-based versatile and stiffness-tunable soft gripper integrating soft pneumatic fingers and wrist, *Soft Robot.* 6 (1) (2019) 1–20.
- [10] Z. Xie, F. Yuan, J. Liu, L. Tian, B. Chen, Z. Fu, S. Mao, T. Jin, Y. Wang, X. He, G. Wang, Y. Mo, X. Ding, Y. Zhang, C. Laschi, L. Wen, Octopus-inspired sensorized soft arm for environmental interaction, *Sci. Robot.* 8 (84) (2023) eadh7852.
- [11] Z. Fang, Y. Wu, Y. Su, J. Yi, S. Liu, Z. Wang, Omnidirectional compliance on cross-linked actuator coordination enables simultaneous multi-functions of soft modular robots, *Sci. Rep.* 13 (1) (2023) 12116.
- [12] A.D. Marchese, C.D. Onal, D. Rus, Autonomous soft robotic fish capable of escape maneuvers using fluidic elastomer actuators, *Soft Robot.* 1 (1) (2014) 75–87.
- [13] M.S. Xavier, C.D. Tawk, A. Zolfagharian, J. Pinskiert, D. Howard, T. Young, J. Lai, S.M. Harrison, Y.K. Yong, M. Bodaghi, A.J. Fleming, Soft pneumatic actuators: A review of design, fabrication, modeling, sensing, control and applications, *IEEE Access* 10 (2022) 59442–59485.
- [14] D. Rus, M.T. Tolley, Design, fabrication and control of soft robots, *Nature* 521 (7553) (2015) 467–475.
- [15] M. Feng, D. Yang, L. Ren, G. Wei, G. Gu, X-crossing pneumatic artificial muscles, *Sci. Adv.* 9 (38) (2023) eadi7133.
- [16] T. Wang, L. Ge, G. Gu, Programmable design of soft pneu-net actuators with oblique chambers can generate coupled bending and twisting motions, *Sensors Actuators A: Phys.* 271 (2018) 131–138.
- [17] F. Connolly, C.J. Walsh, K. Bertoldi, Automatic design of fiber-reinforced soft actuators for trajectory matching, *Proc. Natl. Acad. Sci.* 114 (1) (2017) 51–56.
- [18] N. Gariya, S. Kumar, A. Shaikh, B. Prasad, H. Nautiyal, A review on soft pneumatic actuators with integrated or embedded soft sensors, *Sensors Actuators A: Phys.* 372 (2024) 115364.
- [19] Z. Fang, S. Tang, Y. Su, X. Liu, S. Liu, J. Yi, Z. Wang, J.S. Dai, 3D printed multi-cavity soft actuator with integrated motion and sensing functionalities via bio-inspired interweaving foldable endomysium, *Adv. Sci.* (2024) 2409060.
- [20] T.G. Thuruthel, B. Shih, C. Laschi, M.T. Tolley, Soft robot perception using embedded soft sensors and recurrent neural networks, *Sci. Robot.* 4 (26) (2019) eaav1488.
- [21] Y. Li, Y. Chen, Y. Yang, Y. Wei, Passive particle jamming and its stiffening of soft robotic grippers, *IEEE Trans. Robot.* 33 (2) (2017) 446–455.
- [22] Z. Zhang, G. Chen, Y. Xun, Y. Long, J. Wang, H. Wang, J. Angeles, Bioinspired rigid-soft hybrid origami actuator with controllable versatile motion and variable stiffness, *IEEE Trans. Robot.* 39 (6) (2023) 4768–4784.
- [23] M. Pontin, D.D. Damian, Multimodal soft valve enables physical responsiveness for preemptive resilience of soft robots, *Sci. Robot.* 9 (92) (2024) eadk9978.
- [24] Y. Zhai, A.D. Boer, J. Yan, B. Shih, M. Faber, J. Speros, R. Gupta, M.T. Tolley, Desktop fabrication of monolithic soft robotic devices with embedded fluidic control circuits, *Sci. Robot.* 8 (2023) eadg3792.
- [25] A. Heiden, D. Preninger, L. Lehner, M. Baumgartner, M. Drack, E. Woritzka, D. Schiller, R. Gerstmayr, F. Hartmann, M. Kaltenbrunner, 3D printing of resilient biogels for omnidirectional and exteroceptive soft actuators, *Sci. Robot.* 7 (63) (2022) eabk2119.
- [26] M. Lalegani Dezaki, M. Bodaghi, A review of recent manufacturing technologies for sustainable soft actuators, *Int. J. Precis. Eng. Manufacturing-Green Technol.* 10 (6) (2023) 1661–1710.
- [27] D. Bruder, M.A. Graule, C.B. Teeple, R.J. Wood, Increasing the payload capacity of soft robot arms by localized stiffening, *Sci. Robot.* 8 (81) (2023) eadf9001.
- [28] Y. Su, Z. Fang, W. Zhu, X. Sun, Y. Zhu, H. Wang, K. Tang, H. Huang, S. Liu, Z. Wang, A high-payload proprioceptive hybrid robotic gripper with soft origamic actuators, *IEEE Robot. Autom. Lett.* 5 (2) (2020) 3003–3010.
- [29] M. Fatahillah, N. Oh, H. Rodrigue, A novel soft bending actuator using combined positive and negative pressures, *Front. Bioeng. Biotechnol.* 8 (2020) 472.
- [30] T. Wen, J. Hu, J. Zhang, X. Li, S. Kang, N. Zhang, Design, performance analysis, and experiments of a soft robot for rescue, *J. Mech. Robot.* 16 (071011) (2023).
- [31] B. Tondu, Modelling of the McKibben artificial muscle: A review, *J. Intell. Mater. Syst. Struct.* 23 (3) (2012) 225–253.
- [32] G. Adele, 3D-printed biomimetic artificial muscles using soft actuators that contract and elongate, *Sci. Robot.* (2022).
- [33] S. Li, D.M. Vogt, D. Rus, R.J. Wood, Fluid-driven origami-inspired artificial muscles, *Proc. Natl. Acad. Sci.* 114 (50) (2017) 13132–13137.
- [34] X. Liu, Y. Zhao, D. Geng, S. Chen, X. Tan, C. Cao, Soft humanoid hands with large grasping force enabled by flexible hybrid pneumatic actuators, *Soft Robot.* 8 (2) (2021) 175–185.
- [35] S. Chen, F. Chen, Z. Cao, Y. Wang, Y. Miao, G. Gu, X. Zhu, Topology optimization of skeleton-reinforced soft pneumatic actuators for desired motions, *IEEE/ASME Trans. Mechatronics* 26 (4) (2021) 1745–1753.
- [36] X. Dong, C. Tang, S. Jiang, Q. Shao, H. Zhao, Increasing the payload and terrain adaptivity of an untethered crawling robot via soft-rigid coupled linear actuators, *IEEE Robot. Autom. Lett.* 6 (2) (2021) 2405–2412.
- [37] H. Li, J. Yao, P. Zhou, X. Chen, Y. Xu, Y. Zhao, High-force soft pneumatic actuators based on novel casting method for robotic applications, *Sensors Actuators A: Phys.* 306 (2020) 111957.
- [38] Y. Long, X. Zhu, P. Shi, Q. Liu, Y. Wang, H. Wang, G. Chen, A high-performance elastic-soft hybrid pneumatic actuator with origami structure, *Int. J. Mech. Sci.* 2025 (2025) 109935.
- [39] S. Liu, J. Liu, K. Zou, X. Wang, Z. Fang, J. Yi, Z. Wang, A six degrees-of-freedom soft robotic joint with tilt-arranged origami actuator, *J. Mech. Robot.* 14 (6) (2022) 060912.
- [40] D. Li, D. Fan, R. Zhu, Q. Lei, Y. Liao, X. Yang, Y. Pan, Z. Wang, Y. Wu, S. Liu, H. Wang, Origami-inspired soft twisting actuator, *Soft Robot.* 10 (2) (2023) 395–409.
- [41] C. Zhang, Z. Zhang, Y. Peng, Y. Zhang, S. An, Y. Wang, Z. Zhai, Y. Xu, H. Jiang, Plug & play origami modules with all-purpose deformation modes, *Nat. Commun.* 14 (1) (2023) 4329.
- [42] L. Paez, G. Agarwal, J. Paik, Design and analysis of a soft pneumatic actuator with origami shell reinforcement, *Soft Robot.* 3 (3) (2016) 109–119.
- [43] H. Chen, Y. Ma, W. Chen, Design and optimization of an origami-inspired foldable pneumatic actuator, *IEEE Robot. Autom. Lett.* 9 (2) (2024) 1278–1285.
- [44] X. Zou, T. Liang, M. Yang, C. LoPresti, S. Shukla, M. Akin, B.T. Weil, S. Hoque, E. Gruber, A.D. Mazzeo, Paper-based robotics with stackable pneumatic actuators, *Soft Robot.* 9 (3) (2022) 542–551.
- [45] A. Zaghloul, G.M. Bone, Origami-inspired soft pneumatic actuators: generalization and design optimization, *Actuators* 12 (2) (2023) 72.
- [46] J. Yi, X. Chen, C. Song, Z. Wang, Fiber-reinforced origamic robotic actuator, *Soft Robot.* 5 (1) (2018) 81–92.
- [47] J. Yi, X. Chen, C. Song, J. Zhou, Y. Liu, S. Liu, Z. Wang, Customizable three-dimensional-printed origami soft robotic joint with effective behavior shaping for safe interactions, *IEEE Trans. Robot.* 35 (1) (2019) 114–123.
- [48] M.S. Xavier, C.D. Tawk, Y.K. Yong, A.J. Fleming, 3D-printed omnidirectional soft pneumatic actuators: Design, modeling and characterization, *Sensors Actuators A: Phys.* 332 (2021) 113199.

- [49] J. Xiong, Y. Luo, F. Guan, X. Zhao, Y. Zeng, G. Wei, X. Sun, C. Liu, Bioinspired soft actuators for high bending stiffness and flexible spatial locomotion, *IEEE Robot. Autom. Lett.* 9 (11) (2024) 10391–10398.
- [50] K. Lee, K. Bayarsaikhan, G. Aguilar, J. Realmuto, J. Sheng, Design and characterization of soft fabric omnidirectional bending actuators, *Actuators* 13 (3) (2024) 112.
- [51] J. Walker, T. Zidek, C. Harbel, S. Yoon, F.S. Strickland, S. Kumar, M. Shin, Soft robotics: A review of recent developments of pneumatic soft actuators, *Actuators* 9 (1) (2020) 3.
- [52] B. Wang, T. Yu, Numerical investigation of novel 3D-SPA for gripping analysis in multi-environment, *Int. J. Mech. Sci.* 240 (2023) 107916.
- [53] X. Huang, Y. Rong, G. Gu, High-precision dynamic control of soft robots with the physics-learning hybrid modeling approach, *IEEE/ASME Trans. Mechatronics* (2024) 1–12.
- [54] G. Zhong, W. Dou, X. Zhang, H. Yi, Bending analysis and contact force modeling of soft pneumatic actuators with pleated structures, *Int. J. Mech. Sci.* 193 (2021) 106150.
- [55] Y. Zhu, M. Schenk, E.T. Filipov, A review on origami simulations: from kinematics, to mechanics, toward multiphysics, *Appl. Mech. Rev.* 74 (2022) 030801.
- [56] G. Wei, J.S. Dai, Origami-inspired integrated planar-spherical overconstrained mechanisms, *J. Mech. Des.* 136 (5) (2014) 051003.
- [57] H. Feng, R. Peng, J. Ma, Y. Chen, Rigid foldability of generalized triangle twist origami pattern and its derived 6R linkages, *J. Mech. Robot.* 10 (5) (2018) 051003.
- [58] L. Zimmermann, K. Shea, T. Stanković, Conditions for rigid and flat foldability of degree-n vertices in origami, *J. Mech. Robot.* 12 (1) (2020) 011020.
- [59] Y. Chen, R. Peng, Z. You, Origami of thick panels, *Science* 349 (6246) (2015) 396–400.
- [60] W. Wu, Z. You, Modelling rigid origami with quaternions and dual quaternions, *Proc.: Math. Phys. Eng. Sci.* 466 (2119) (2010) 2155–2174.
- [61] S. Liu, G. Lu, Y. Chen, Y.W. Leong, Deformation of the miura-ori patterned sheet, *Int. J. Mech. Sci.* 99 (2015) 130–142.
- [62] L. Yuan, H. Dai, J. Song, J. Ma, Y. Chen, The behavior of a functionally graded origami structure subjected to quasi-static compression, *Mater. Des.* 189 (2020) 108494.
- [63] Y. Zhu, E.T. Filipov, A bar and hinge model for simulating bistability in origami structures with compliant creases, *J. Mech. Robot.* 12 (2) (2020) 021110.
- [64] E. Filipov, K. Liu, T. Tachi, M. Schenk, G. Paulino, Bar and hinge models for scalable analysis of origami, *Int. J. Solids Struct.* 124 (2017) 26–45.
- [65] H. Zhang, H. Feng, J.-L. Huang, J. Paik, Generalized modeling of origami folding joints, *Extrem. Mech. Lett.* 45 (2021) 101213.
- [66] H. Soleimani, T. Goudarzi, M. Aghdam, Advanced structural modeling of a fold in origami/kirigami inspired structures, *Thin-Walled Struct.* 161 (2021) 107406.
- [67] S.R. Woodruff, E.T. Filipov, A bar and hinge model formulation for structural analysis of curved-crease origami, *Int. J. Solids Struct.* 204–205 (2020) 114–127.
- [68] T.-U. Lee, Z. You, J.M. Gattas, Elastica surface generation of curved-crease origami, *Int. J. Solids Struct.* 136–137 (2018) 13–27.
- [69] M.A. Dias, L.H. Dudte, L. Mahadevan, C.D. Santangelo, Geometric mechanics of curved crease origami, *Phys. Rev. Lett.* 109 (11) (2012) 114301.
- [70] S. Liu, F. Chen, D. Duanmu, Y. Wang, J. Liu, W. Yang, Y. Zhu, Y. Wu, J. Yi, J.S. Dai, Z. Wang, Small-strain folding of semi-rigid elastomer derives high-performance 3D-printable soft origami actuators, *Chem. Eng. J.* 489 (2024) 151462.
- [71] F. Daerden, D. Lefevere, The concept and design of pleated pneumatic artificial muscles, *Int. J. Fluid Power* 2 (3) (2001) 41–50.
- [72] J.W. Ambrose, N.Z.R. Chiang, D.S.Y. Cheah, C.-H. Yeow, Compact multilayer extension actuators for reconfigurable soft robots, *Soft Robot.* 10 (2) (2023) 301–313.
- [73] M.A. Robertson, H. Sadeghi, J.M. Florez, J. Paik, Soft pneumatic actuator fascicles for high force and reliability, *Soft Robot.* 4 (1) (2017) 23–32.